nature portfolio

https://doi.org/10.1038/s41586-022-05393-7

Supplementary information

Ultrathin quantum light source with van der Waals $NbOCl_2$ crystal

In the format provided by the authors and unedited

Supplementary materials for

Ultrathin quantum light source with van der Waals $NbOCl_2$ crystal

Qiangbing Guo[1,2,3,14,*], Xiao-Zhuo Qi[4,5,14], Lishu Zhang[6,14], Meng Gao[7,14], Sanlue Hu[8], Wenju Zhou[9], Wenjie Zang[1], Xiaoxu Zhao[10], Junyong Wang[3,6], Bingmin Yan[9], Mingquan Xu[7], Yun-Kun Wu[4,5], Goki Eda[3,6], Zewen Xiao[8], Shengyuan A. Yang[11], Huiyang Gou[9], Yuan Ping Feng[3,6], Guang-Can Guo[4,5,12], Wu Zhou[7,13], Xi-Feng Ren[4,5,12,*], Cheng-Wei Qiu[1,3*], Stephen J. Pennycook[2,7,*] and Andrew T. S. Wee[3,6,*]

[1]Department of Electrical and Computer Engineering, National University of Singapore, Singapore, Singapore.

[2]Department of Materials Science and Engineering, National University of Singapore, Singapore, Singapore.

[3]Centre for Advanced 2D Materials and Graphene Research Centre, National University of Singapore, Singapore, Singapore.

[4]CAS Key Laboratory of Quantum Information, University of Science and Technology of China, Hefei, China.

[5]CAS Center for Excellence in Quantum Information and Quantum Physics, University of Science and Technology of China, Hefei, China.

[6]Department of Physics, National University of Singapore, Singapore, Singapore.

[7]School of Physical Sciences and CAS Key Laboratory of Vacuum Physics, University of Chinese Academy of Sciences, Beijing, China.

[8]Wuhan National Laboratory for Optoelectronics, Huazhong University of Science and Technology, Wuhan, China.

[9]Center for High Pressure Science and Technology Advanced Research, Beijing, China.

[10]School of Materials Science and Engineering, Peking University, Beijing, China.

[11]Research Laboratory for Quantum Materials, Singapore University of Technology and Design, Singapore, Singapore.

[12]Hefei National Laboratory, University of Science and Technology of China, Hefei, China.

[13]CAS Center for Excellence in Topological Quantum Computation, University of Chinese Academy of Sciences, Beijing, China.

[14]These authors contributed equally: Qiangbing Guo, Xiao-Zhuo Qi, Lishu Zhang, Meng Gao..

*qbguo90@hotmail.com (Q.G.); renxf@ustc.edu.cn (X.-F.R.); chengwei.qiu@nus.edu.sg (C.-W.Q.); stephen.pennycook@cantab.net (S.J.P.); phyweets@nus.edu.sg (A.T.S.W.).

S1. Additional structural characterizations

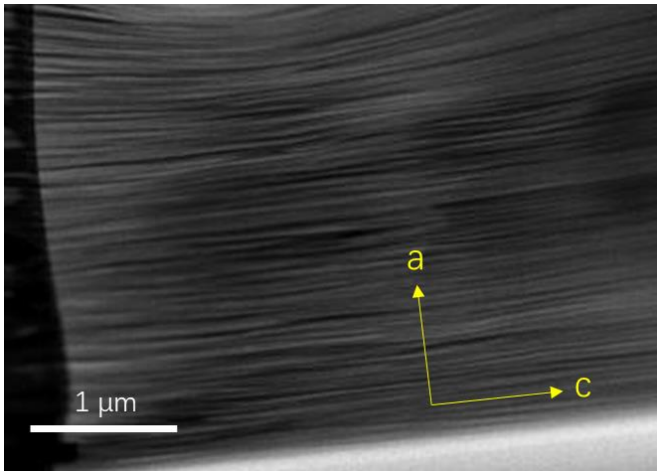

Figure S1 | HAADF image of the $NbOCl_2$ crystal. A 2D layered structure can be clearly seen.

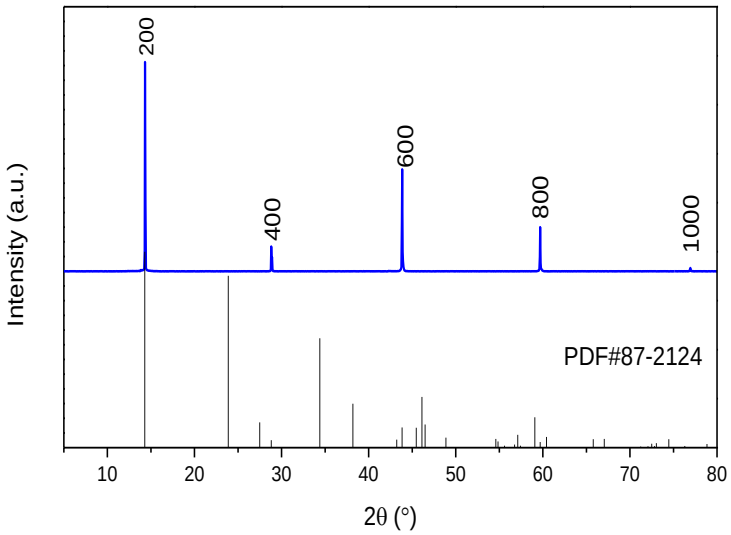

Figure S2 | XRD of the synthesized single crystal. The diffraction pattern shows a preferred crystal orientation along the *a*-axis and matches well with the standard PDF card (#87-2124) of $NbOCl_2$ crystal.

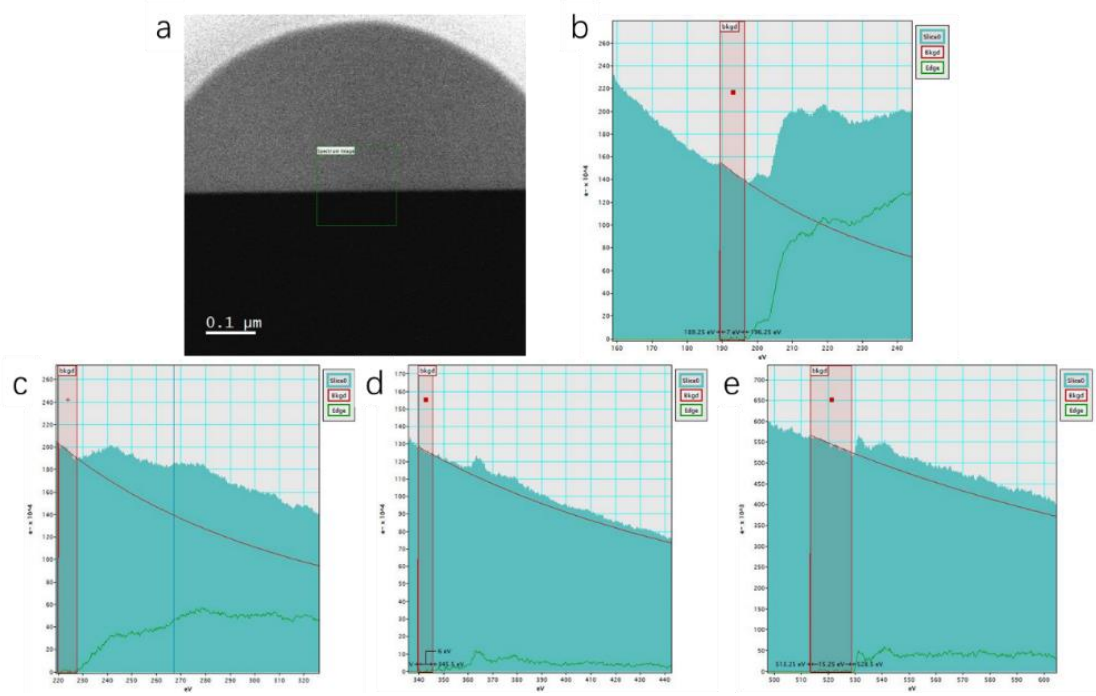

Figure S3 | Additional EELS data related to the EELS elemental mapping image (Figure 1g, main text). a, HAADF-STEM image of a thin flake. The green box indicates the area where the EELS data was collected. **b-e**, Original EEL spectra, which confirm the coexistence of Cl, O, and Nb. The spectra in (**b-e**) are averaged over the green square in (**a**), showing the Cl-$L_{2,3}$, O-*K*, Nb-$M_{4,5}$, and Nb-$M_{2,3}$ edges, respectively. The background showing in red was subtracted by the power law model with Digital Micrograph software, and the stripped edges are shown in green.

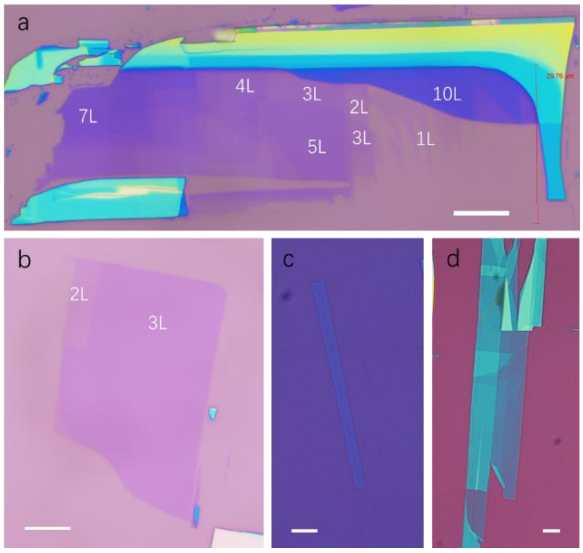

Figure S4 | Optical images of exfoliated flakes on silicon substrates. Scale bar, 10 μm. It is easy

to exfoliate the $NbOCl_2$ crystals by commonly used scotch tape method. (**a-d**) Thin and anisotropic flakes down to monolayer can be easily obtained, implying a weak interlayer coupling and high in-plane structural anisotropy.

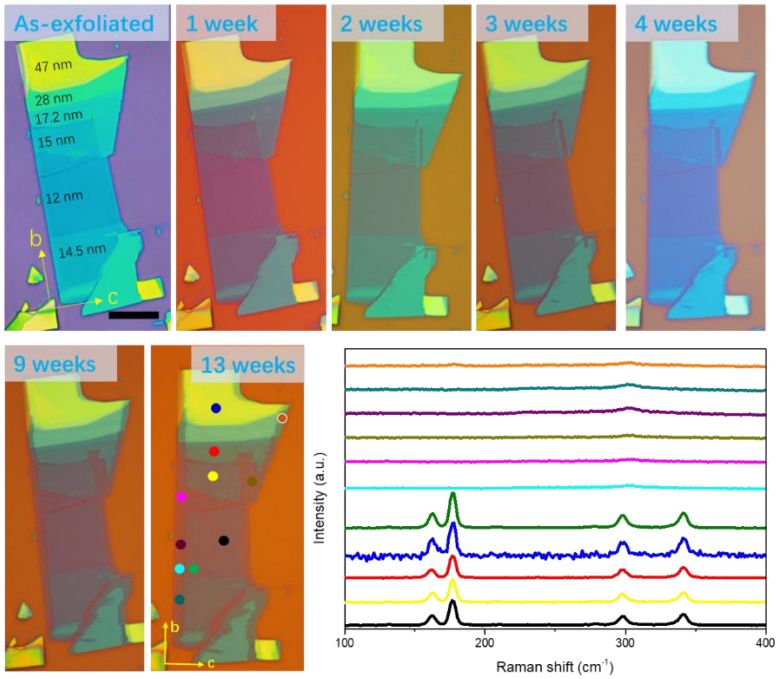

Figure S5 | Stability of a typical exfoliated $NbOCl_2$ thin flake under ambient conditions. Scale bar, 10 μm. No detectable change was observed in the first week after exfoliation. But slight change at the edge could be noted from the second week and gradually become obvious with time. It is interesting to find that the degradation only happens at one edge side (parallel to the *b*-axis) and gradually developed to the middle in a direction along the *c*-axis, while the other edge (parallel to the *c*-axis) remained almost no change after 13 weeks. From the optical microscope images, the degraded edges show different optical contrast and can be easily identified. Raman spectra (bottom right, the same color code with the dots in the left image) show that no characteristic Raman peaks can be observed in the degraded area, while the Raman signals remain no change in the middle area. The structural change of the degraded area can be found in Figure S6 below.

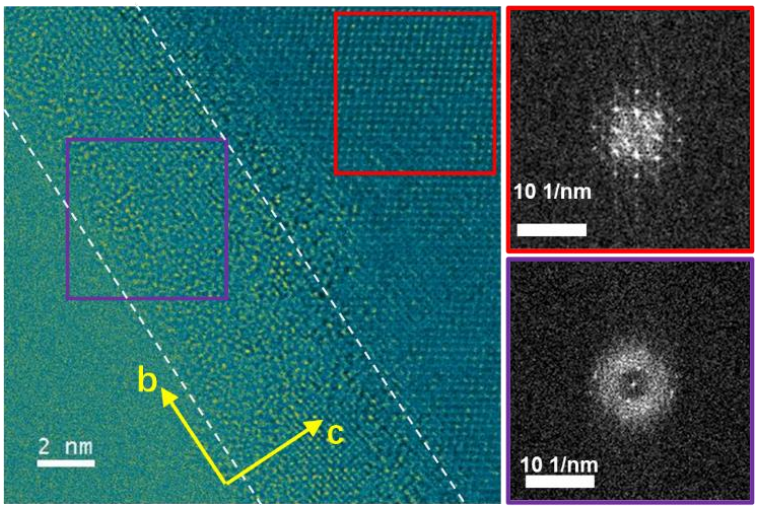

Figure S6 | STEM image of an edge-degraded thin flake and corresponding fast Fourier transform patterns of the edge and middle areas. Diffraction spot pattern can be observed in the middle area, indicating a crystalline nature; while a diffraction loop is in the edge area, indicating an amorphous nature. In other word, the edge degraded into amorphous state, which is consistent with the featureless Raman response (Figure S5 above). As for the detailed mechanism of degradation, more in-depth investigations are needed and will be our future work.

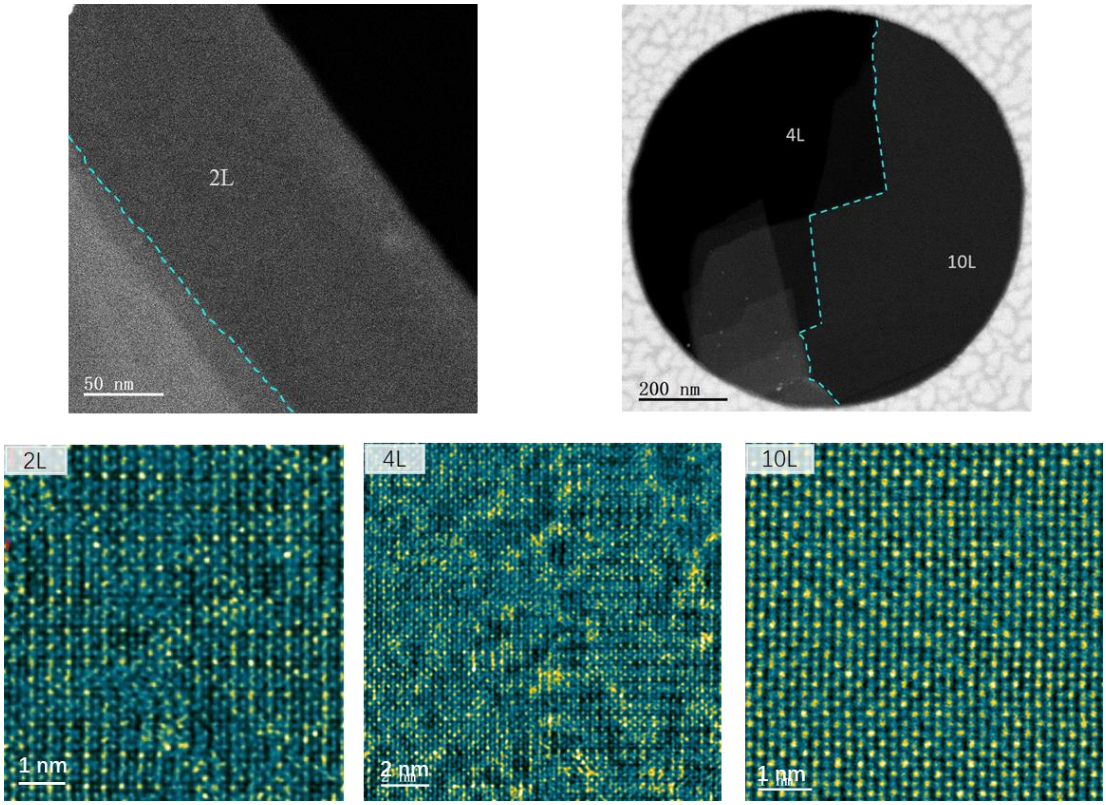

Figure S7 | STEM images of thin flakes after collecting the valence EELS data. The corresponding STEM images all demonstrate a well remained crystalline state after valence EELS data collections, excluding damage induced by electron beam, and therefore ensures the reliability of the EELS data.

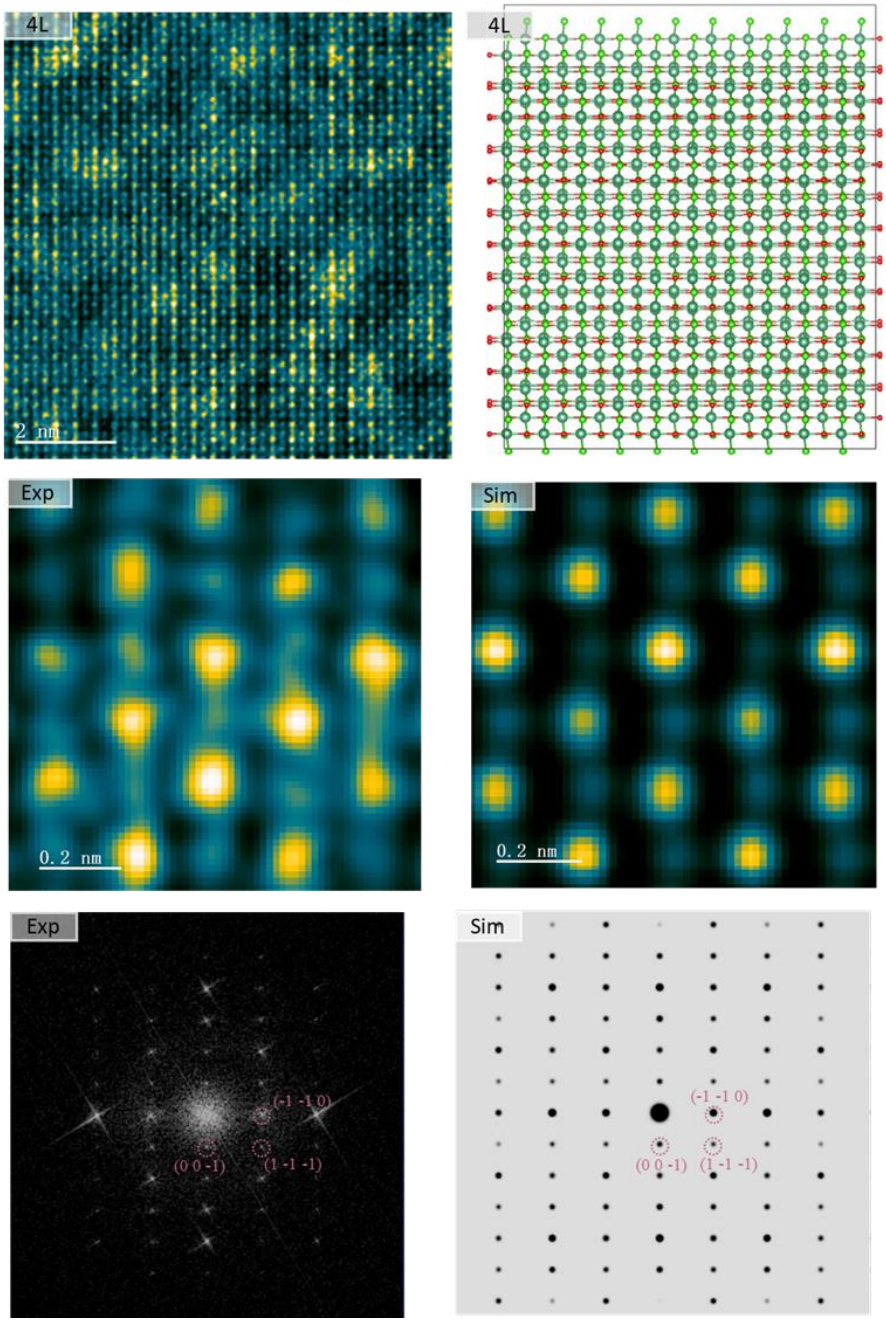

Figure S8 | Typical in-plane STEM characterizations of a 4-layer sample. In-plane atomic-resolution ADF-STEM images (middle panel is the enlarged image from upper panel) and corresponding Fast Fourier transform (FFT) pattern (bottom panel) of a 4-layer flake, along with their corresponding simulated ones (right column). Clearly, the atomic images are in perfect match with the simulated ones based on perfect crystal structure model. No moire pattern or additional point in FFT pattern was observed, thus excluding the existence of stacking faults.

S2. Additional electronic structure and optical transition analysis

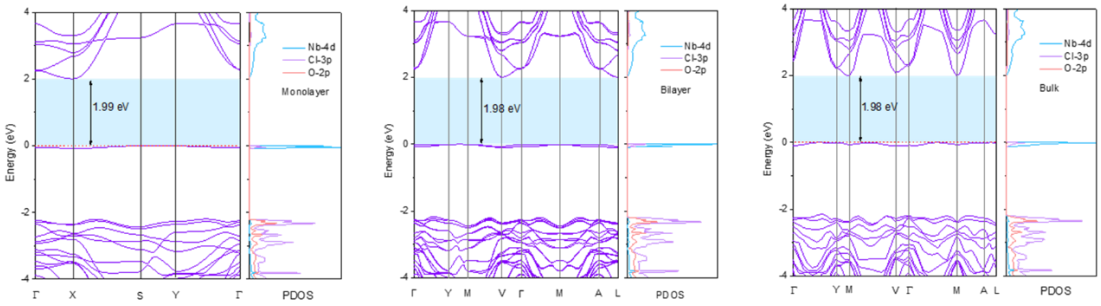

Figure S9 | Calculated electronic structures and projected density of states (PDOS) for monolayer (d), bilayer (e) and bulk (f), respectively, based on HSE hybrid functional. A layer-insenstive bandgap is clear at the HSE level.

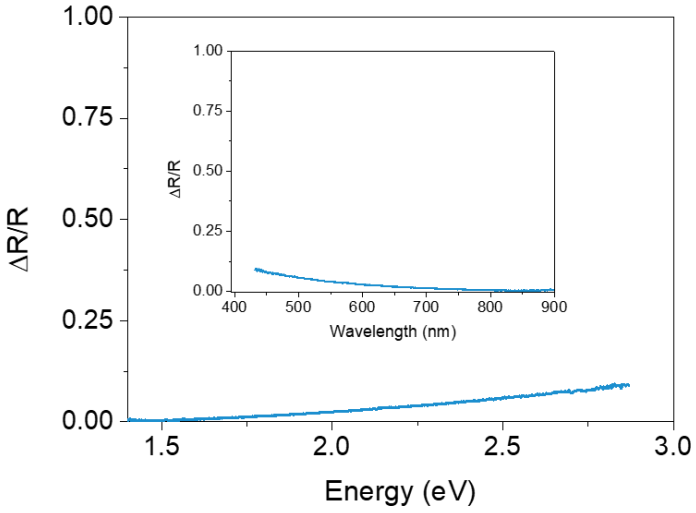

Figure S10 | Experimental absorption spectrum. Inset is the absorption spectrum plotted in a wavelength scale. The absorption spectrum indeed demonstrates a slight absorption onset from ~1.5 eV, which is well consistent with the experimental EELS data and GW-BSE calculation results in Figures 2a and 2f, respectively, in the main text.

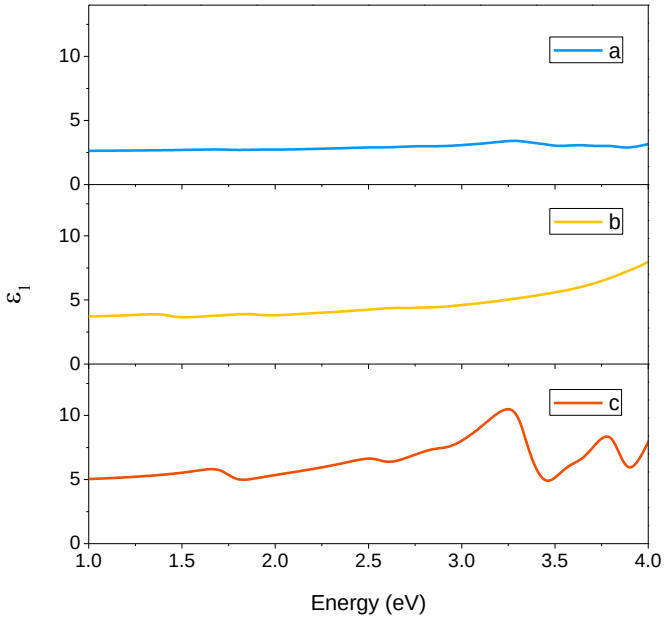

Figure S11 | Real part of dielectric constants along different crystallographic axis.

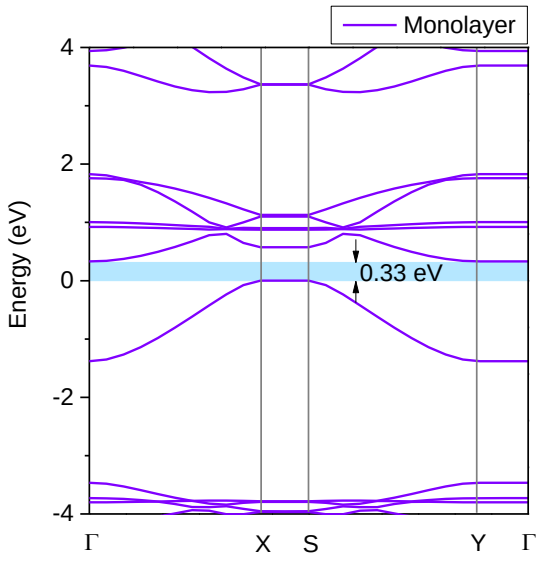

Figure S12 | Calculated electronic structure of a monolayer model structure without Peierls distortion, by DFT-HSE method. It is clear that both bandgap value and VBM have changed significantly compared with the monolayer with Peierls distortion in Figure S9 above (both by DFT-HSE method), indicating the unique role of Peierls distortion in shaping the electronic structure and inducing localized electronic states around VBM.

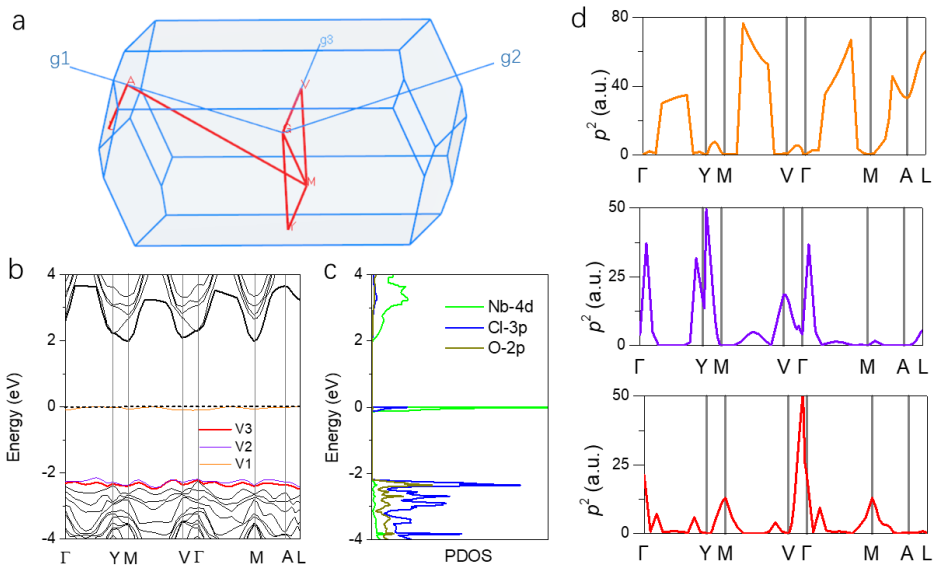

Figure S13 | Optical transition analysis. a, *k*-point path for the monoclinic Brillouin zone. **b**, Calculated electronic structure for bulk crystal (by DFT-HSE), where the three orbitals round the top valence band are highlighted and denoted as V1, V2 and V3, along with the conduction band minimum (CBM) in bold. **c**, The corresponding projected density of states (PDOS). **d**, Calculated optical transition probabilities from V1, V2 and V3 to CBM (same color code as in **b**).

As shown in **b** and **c**, the V1 orbital is mainly contributed by Nb-*4d* states (in addition to a small part of Cl-*3p* states), which are dispersionless and quite localized in energy. The optical transitions from localized Nb-*4d* states (V1) to empty Nb-*4d* orbitals in the conduction band (the Nb-*4d* states also dominate the CBM as shown in **b**) are forbidden based on the selection rules, which is manifested by the nearly zero transition probability at M point that corresponds to the optical transition to CBM (upper panel in **d**). V2 also demonstrates a near zero optical transition probability (middle panel in **d**). A large probability happens for V3, indicating an allowed optical transition from V3 to CBM. In other word, optical transitions from VBM (V1 orbitals) are quite suppressed by the localized Nb-*4d* states around VBM (though with considerable DOS), whereas significant optical transitions mainly come from V3 orbitals to CBM.

S3. Additional data of interlayer properties

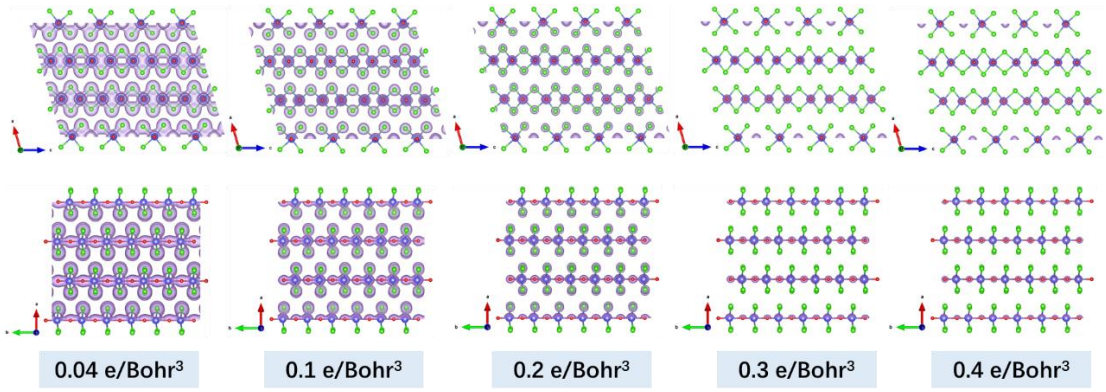

Figure S14 | Interlayer charge density at different isosurface values. Clearly, the electrons are mainly localized on the Nb and O atoms in the intralayer with negligible distribution in the interlayer region, indicating a mainly in-plane bonding.

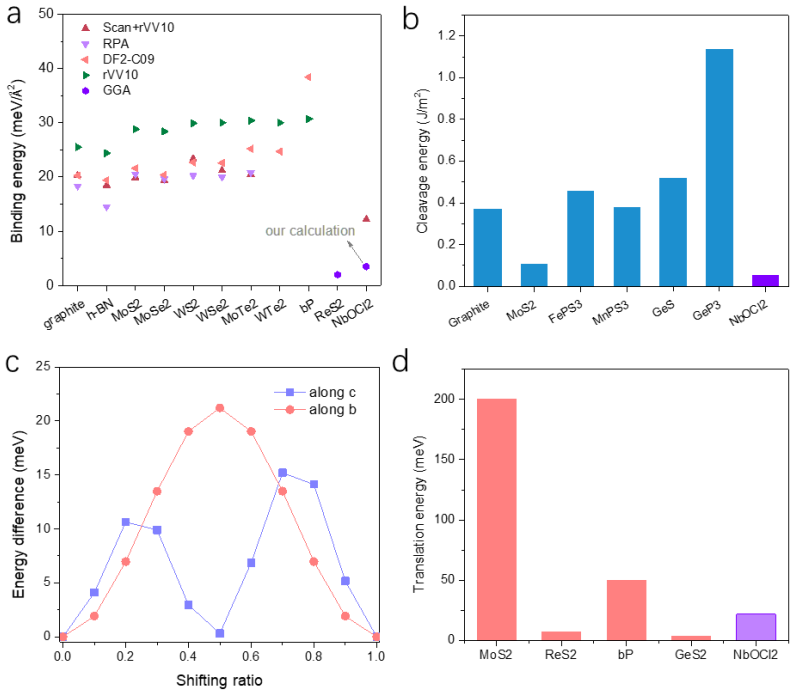

Figure S15 | Additional data of interlayer binding energy (a), cleavage energy (b) and translation energy (c,d). Note that bP represents black phosphorus.

As it is difficult to directly measure the interlayer interaction energy, most of the information are provided by theory calculations. As shown in Figure S15a, binding energy values calculated by different methods (RPA[1], SCAN+rVV10[2], DF2-C09[3] and GGA[4]) for various materials, as well as our calculation result for $NbOCl_2$ here, are presented for comparison. It's noted that different calculation methods will give slightly different values, but a qualitative and reasonable comparison can be conducted. Clearly, an obvious weak interlayer binding energy, especially compared with TMDCs and bP, indeed exists in $NbOCl_2$, which is comparable to that of ReS_2 (another weak interlayer coupling 2D material)[5].

The cleavage energy was also calculated to reveal more information of interlayer interaction. As shown in Figure S15b, the cleavage energy (0.055 J/m^2) also exhibits a low level compared with other 2D materials[5-7], being consistent with the easy experimental exfoliation.

Figure S15c shows the energy difference calculated by translating one $NbOCl_2$ monolayer over another along two crystallographic directions, respectively. Translation energy of ~22 meV along the *b*-axis and ~15 meV along the *c*-axis are derived, which are also much smaller than that of MoS_2 and bP, though slightly higher than that of ReS_2 and GeS_2 that are also interlayer decoupled[5-7].

Therefore, the above results figure out more weak interlayer interaction characters for $NbOCl_2$, in addition to the interlayer electronic decoupling in the main text.

S4. Lattice vibrational properties

In this section, the lattice vibrational information mainly derived from Raman spectra is presented, along with related information and discussions on interlayer vibrational coupling.

Firstly, Raman spectroscopy was performed on flakes with various thicknesses (Figure S16a, on silicon substrate) and five clear Raman peaks (denoted as P1 to P5) were observed for all layers (except for the monolayer as the signal is too weak to detect on a silicon substrate). Remarkably, the five Raman peaks show almost no dependence on thickness within the resolution (~0.3 cm^{-1}) of our equipment (Figure S16b), which is different from TMDCs and many other 2D materials where the Raman peak-shift is usually used as an index of layer number. It should be noted that the P3 and P4 peak shifts come from the influence of silicon substrate (see the Raman spectrum of a blank silicon substrate in Figure S16a). This layer-independence of lattice vibrations can be further evidenced by the unnoticeable Raman peak shift of flakes from monolayer to bulk on a gold substrate (Figure S16c), implying a layer-insensitive Raman response.

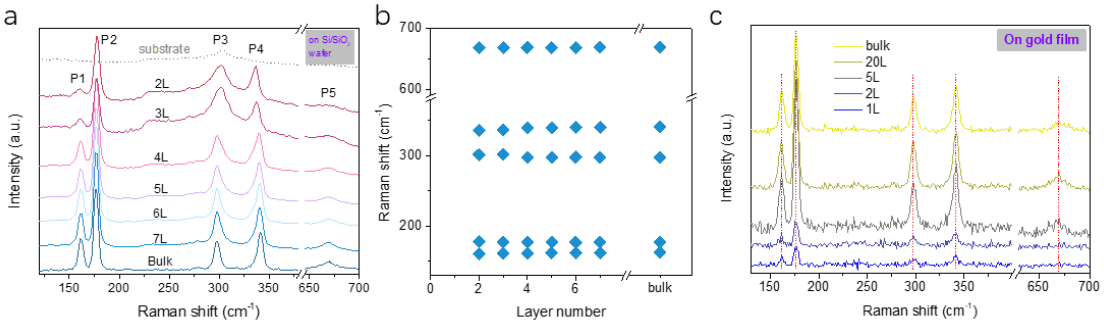

Figure S16 | Raman spectra of flakes with different thickness on silicon substrate (a,b) and gold substrate (c).

As shown in Figure S17 and S18, the lattice vibration also shows a strong in-plane anisotropy, being consistent with the strong in-plane crystallographic anisotropy. To gain more insight into the vibrational properties of each Raman peak, we calculated the phonon modes using DFT.

As $NbOCl_2$ belongs to the space group *C2* and has 8 atoms in the unit cell, it supports 24 phonon modes with 21 Raman-active optical phonons including 11A+10B, where A and B are the

irreducible representations. Table S2 shows the calculated phonon modes with corresponding symmetries. Firstly, we tried to assign the experimental Raman peaks (P1-P5) to the phonon modes according to the Raman activity intensity, while the mode 16 vibration is not obvious at ambient pressure but become comparable with other peaks under pressure (Figure S19). The assignment is verified by the polarized Raman spectra and symmetry analysis as discussed below.

The symmetry of the Raman-active phonons is determined by the Raman tensors (**R**) of the C_2 point group

$$\mathbf{R}(\mathrm{A})=\begin{bmatrix} a & 0 & d \\ 0 & b & 0 \\ d & 0 & c \end{bmatrix}, \mathbf{R}(\mathrm{B})=\begin{bmatrix} 0 & e & 0 \\ e & 0 & f \\ 0 & f & 0 \end{bmatrix},$$

where the *a*, *b*, *c*, *d*, *e*, and *f* are the tensor elements, and their values depend on the cross-section of Raman scattering. When considering the light absorption, the Raman tensor should be as

$$\mathbf{R}(\mathrm{A})=\begin{bmatrix} |a|e^{i\varphi_a} & 0 & |d|e^{i\varphi_d} \\ 0 & |b|e^{i\varphi_b} & 0 \\ |d|e^{i\varphi_d} & 0 & |c|e^{i\varphi_c} \end{bmatrix}, \mathbf{R}(\mathrm{B})=\begin{bmatrix} 0 & |e|e^{i\varphi_e} & 0 \\ |e|e^{i\varphi_e} & 0 & |f|e^{i\varphi_f} \\ 0 & |f|e^{i\varphi_f} & 0 \end{bmatrix},$$

where φ_a is the phase of the Raman tensor element *a*.

As the observed Raman intensity depends on the symmetry selection rules and the scattering geometry. The scattering intensity (***I***) of the Raman-active phonon has the following relationship with the polarization states of incident light $\boldsymbol{e_i}$ and the scattered light $\boldsymbol{e_s}$ and **R**

$$I \propto |e_i \cdot R \cdot e_s|^2. \quad (1)$$

We define the direction along the *c*-axis of crystal as 0 degree (Figure S17b). Under parallel-polarized configuration, $\boldsymbol{e_s = e_i = (0, sin\theta, cos\theta)}$; while under perpendicular configuration, $\boldsymbol{e_s = (0, -cos\theta, sin\theta)}$. Then the Raman intensity of A- and B-symmetry modes in parallel and perpendicular polarization configurations is as follow

$$I_A^{//} \propto |b|^2 cos^4\theta + |c|^2 sin^4\theta + \frac{1}{2}|b||c| sin^2 2\theta \cdot cos\varphi_{c-b} \quad (2)$$

$$I_A^{\perp} \propto \frac{1}{4} sin^2 2\theta \cdot [|b|^2 + |c|^2 - 2|b||c| \cdot cos\varphi_{c-b}] \quad (3)$$

$$I_B^{//} \propto [|f| sin 2\theta]^2 \quad (4)$$

$$I_B^{\perp} \propto [|f| cos 2\theta]^2 \quad (5)$$

where φ_{c-b} is φ_c-φ_b.

Obviously, the polarization-dependent Raman intensity in both configurations for B-symmetry modes will have a period of π/2. However, as shown in Figure S17c-f, the polarization-dependent Raman intensity of all the five observed Raman peaks in the parallel configuration show a period of π. Thus, all the five observed Raman peaks should be attributed to A-symmetry modes.

In the parallel configuration (corresponding to Equation (2)), the five Raman modes show 3 different types of azimuthal periodicity and phase (Figure S17 and S18a). Type 1 (P1; Figure S17c) has a period of π with two global maxima and two local maxima in a period of 2π; Type 2 (P2, P3, P4; Figure S17d-f) has a period of π but without local maxima; Type 3 (P5; Figure S17d) is similar with type 2 but with a phase shift by π/2. The different azimuthal dependence of the A-symmetry phonon modes indicates that the Raman intensity depends on the details of Raman tensor elements. From the experimental results, type 2 and 3 corresponds to the case where $|c|$~0 ($cos^4\theta$ dependence) or $|b|$~0 ($sin^4\theta$ dependence). For type 1, the imaginary part of the Raman tensor should be taken into consideration. Accordingly, the azimuthal dependence of all five peaks can be well fitted by the above equation (2), evidencing the reasonability of the above assignments. And this can be further confirmed by the $sin^2 2\theta$ dependence of all the five peaks in the perpendicular configuration (Figure S18b), as the B-symmetry Raman modes exhibit a $cos^2 2\theta$ dependence (see equation (5)).

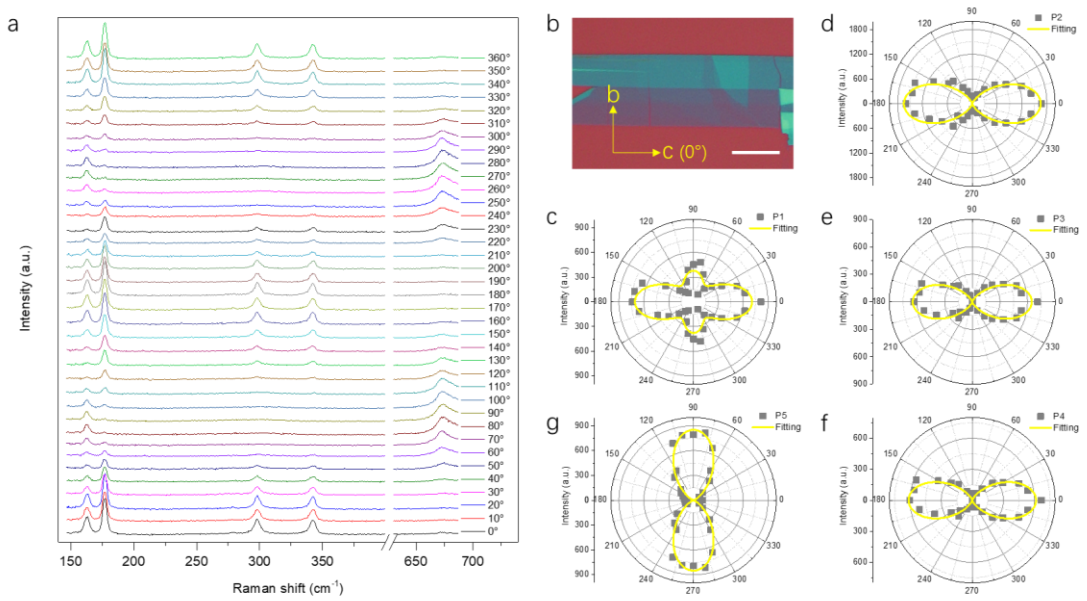

Figure S17 | Polarized Raman Spectra. a, Raman spectra at various polarization angles under parallel configuration. The zero degree is aligned with the crystallographic *c*-axis, as indicated in **b**. **c-g**, Polarization-dependent Raman peak intensity of P1-P5. Scale bar in **b**, 20 μm.

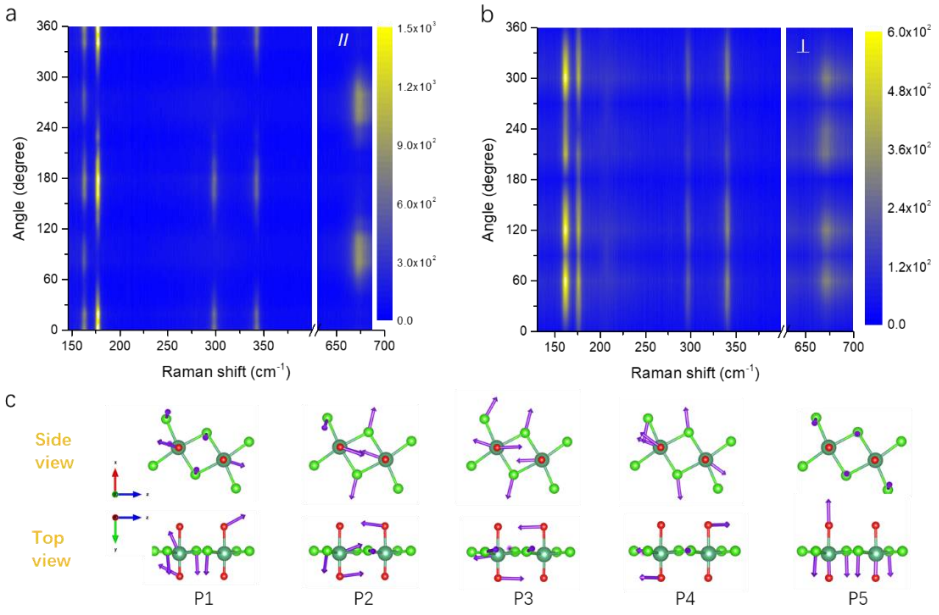

Figure S18 | 2D plot of polarized Raman spectra and Raman-active vibration modes. 2D plot of polarization-dependent Raman spectra under parallel (a) and perpendicular (b) configurations. (c) Side and top views of the atomic displacements for the Raman-active vibration modes.

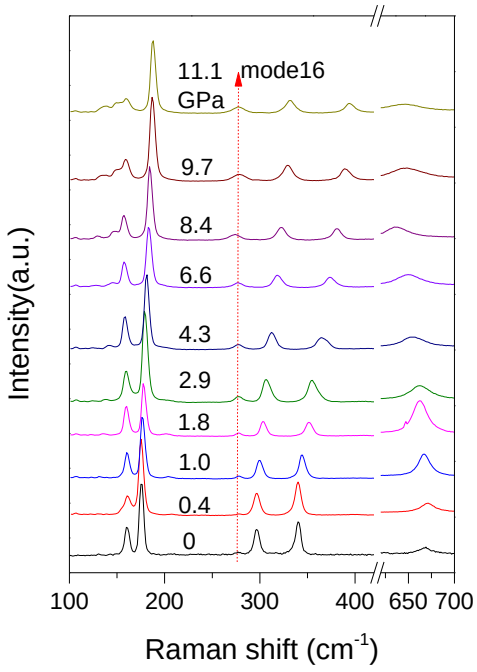

Figure S19 | Raman spectra under various pressure. It is interesting to note that the vibration mode 16 is not obvious at ambient condition but is comparable to P3 and P4 at ~11 GPa, and shows a pressure insensitive character.

To gain an insight into the interlayer vibrational coupling, we performed pressure- and temperature-dependent Raman spectroscopy, with pressure- and temperature-dependent peaks shown in Figures S20a,b, respectively. The most prominent Raman peak P2 corresponds to a mostly out-of-plane vibration mode (see above Raman spectrum analysis and Figure S18c), of which the pressure coefficient (reflects the interlayer coupling[5]) was calculated to be ~0.73 cm^{-1}/GPa while the first-order temperature coefficient χ (also related to the interlayer interactions) was determined to be ~-0.008 cm^{-1}/K by fitting with the Grüneisen model[8]. It's notable that $NbOCl_2$ exhibits the lowest pressure- and temperature-coefficients of the out-of-plane lattice vibration mode among typical 2D materials, being comparable to ReS_2, another well-known weak interlayer-coupling 2D material[5] (Figure S20c). These results also imply a weak interlayer vibrational coupling, though

more detailed investigations are needed to figure out a complete image of the interlayer vibration modes, which will be part of our future work but not the focus of this work.

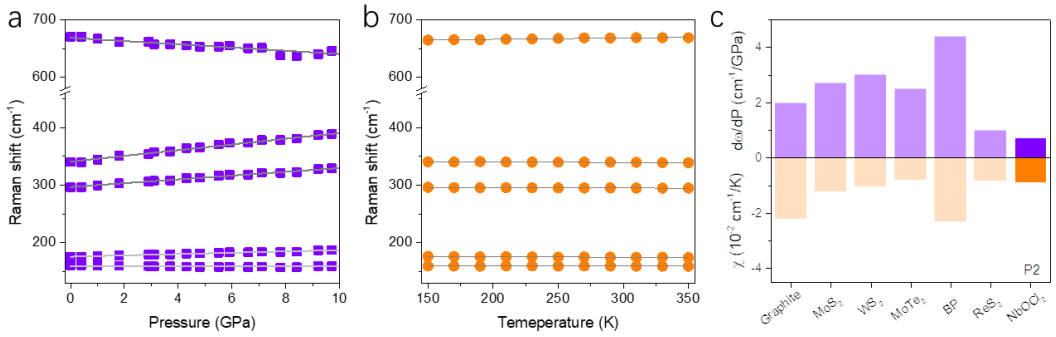

Figure S20 | Pressure and temperature dependent lattice vibration. Pressure (a) and temperature (b) dependent Raman peaks. (c) Comparison of pressure ($d\omega/dP$) and temperature (χ) coefficient of the out-of-plane Raman peaks of typical van der Waals crystals and $NbOCl_2$. More details can be found in Table S3.

S5. Additional SHG data

S5.1 Additional figures

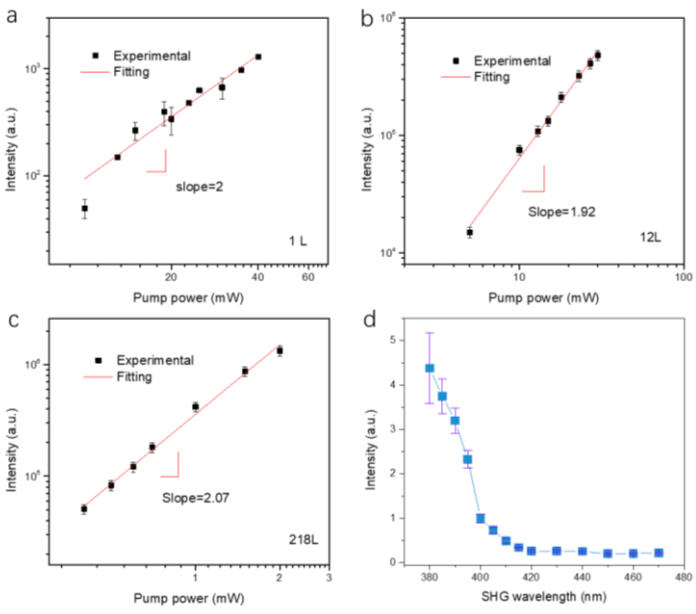

Figure S21 | (a-c) Pump power dependent SHG peak intensity of 1L, 12L, and 218L flakes. All of them can be linearly fitted with a slope of ~2, confirming a second-order nonlinear optical process. (d) Wavelength dependent SHG intensity, indicating an obvious resonance effect at short wavelength region.

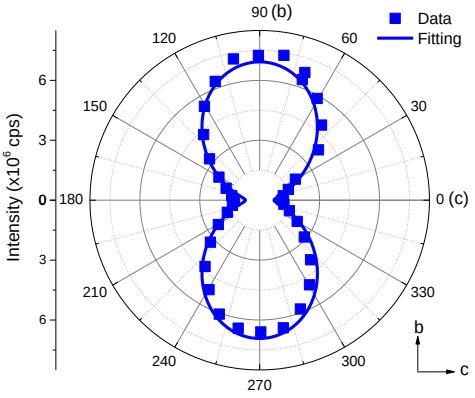

Figure S22 | Overall SHG intensity under different polarization angles of excitation. The zero degree is defined by aligning with the crystallographic *c*-axis and no analyzer was employed before the detector (to collect an overall SHG intensity). The data is well fitted through the symmetry analysis presented below in S5.2**.** The azimuthal dependence of overall SHG intensity is basically different from that of monolayer TMDCs where no polarization dependence is observed (a "O" shape, not the above "8" shape). This dependence is determined by the lower crystal symmetry of $NbOCl_2$ (*C2* space group) than that of monolayer TMDCs (D_{3h}^1), which is analyzed in detail below in S5.2. Remarkably, the high orthorhombic SHG contrast promises much easier crystallographic orientation identification as no optical analyzer is needed, as well as other polarization-related second-order NLO applications that are beyond the reach of TMDCs.

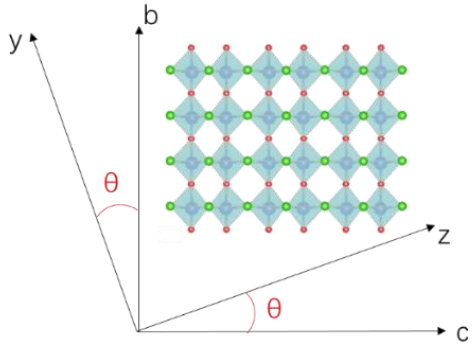

Figure S23 | Demonstration of the transformation from crystal coordinates (*a, b, c*) to laboratory coordinates (*x, y, z*).

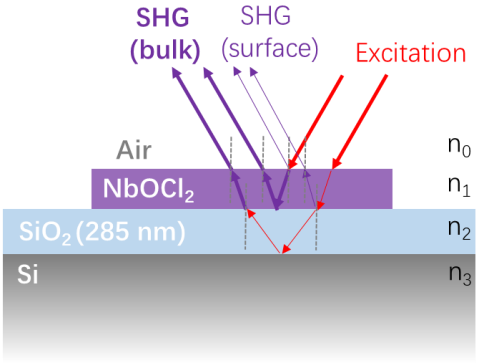

Figure S24 | Schematic illustration of the SHG process under reflection geometry. As we measured SHG on samples exfoliated on silicon substrate (SiO_2(285 nm)/Si), the overall SHG contains the contributions from both bulk and surface ($NbOCl_2$-air)/interface ($NbOCl_2$-SiO_2) effects.

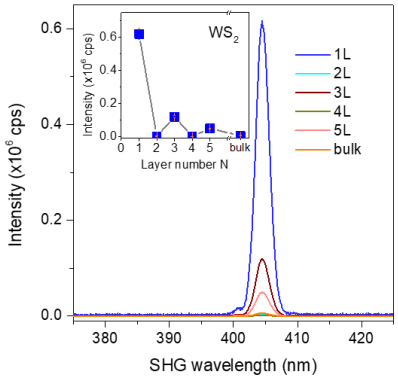

Figure S25 | Layer-dependent SHG of WS_2 at 404 nm (pump=808 nm).

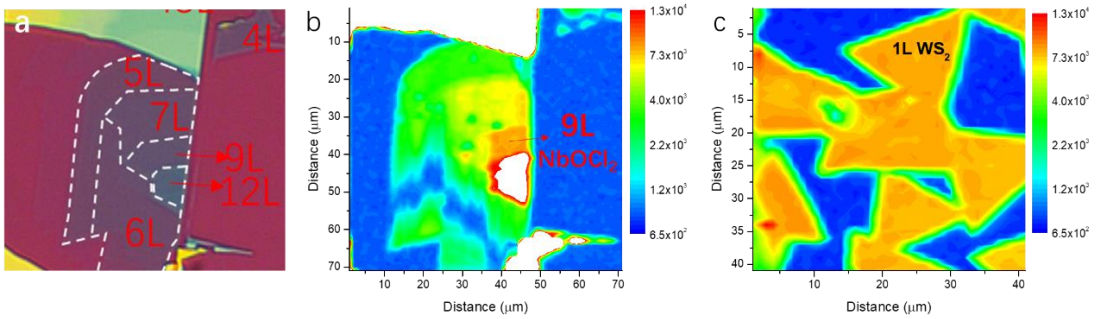

Figure S26 | Direct comparison of SHG intensity. a, Optical microscope image of an exfoliated $NbOCl_2$ flake on silicon substrate with various thicknesses as indicated. **b**, Corresponding SHG intensity mapping of the flake in **a**. **c**, SHG intensity mapping of monolayer WS_2. Both are excited at 808 nm with the same power. The intensity scale bar in **b** and **c** are set in the same range, facilitating a direct comparison. The SHG intensity of monolayer WS_2 is comparable to that of 9L $NbOCl_2$.

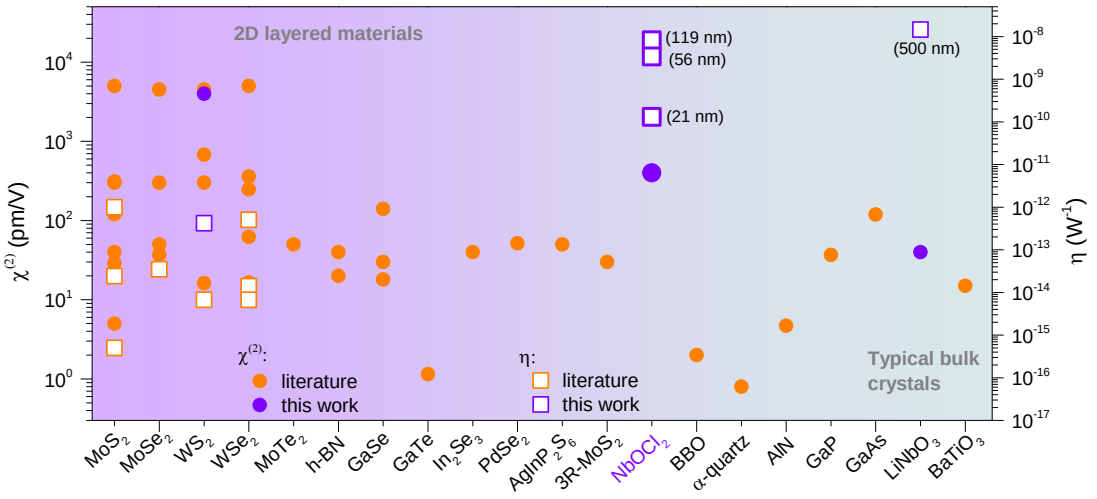

Figure S27 | Comparison of different $\chi^{(2)}$ materials. More detailed information can be found in Table S4 below. The rectangle labels denote nonlinear conversion efficiency, while circle labels denote nonlinear coefficient. Violet color stands for our experimental data while yellow for data from literatures.

S5.2 Polarization-dependent SHG response

In general, the second-harmonic wave at frequency *2ω* when excited with fundamental frequency *ω* can be expressed as

$$P(2\omega)=\begin{bmatrix}P_a(2\omega)\\P_b(2\omega)\\P_c(2\omega)\end{bmatrix}=\begin{bmatrix}\chi_{11}^{(2)} & \chi_{12}^{(2)} & \chi_{13}^{(2)} & \chi_{14}^{(2)} & \chi_{15}^{(2)} & \chi_{16}^{(2)}\\ \chi_{21}^{(2)} & \chi_{22}^{(2)} & \chi_{23}^{(2)} & \chi_{24}^{(2)} & \chi_{25}^{(2)} & \chi_{26}^{(2)}\\ \chi_{31}^{(2)} & \chi_{32}^{(2)} & \chi_{33}^{(2)} & \chi_{34}^{(2)} & \chi_{35}^{(2)} & \chi_{36}^{(2)}\end{bmatrix}\begin{bmatrix}E_a^2\\E_b^2\\E_c^2\\2E_bE_c\\2E_aE_c\\2E_aE_b\end{bmatrix}, \quad (6)$$

where E_a, E_b, and E_c are components of the electrical fields of excitation laser along corresponding crystal axes, and $\chi_{ij}^{(2)}$ is the tensor element of the second-order nonlinear coefficients. *P(2ω)* is the second-order nonlinear polarization.

Provided that in our experiments the electric field of fundamental laser is in the crystallographic *bc* plane, thus $|E_a|$=0. In addition, the crystal belongs to the *C2* space group. the second-order nonlinear coefficient matrix can be expressed as follow (only nonzero elements are listed)

$$\begin{bmatrix}0 & 0 & 0 & \chi_{14}^{(2)} & 0 & \chi_{16}^{(2)}\\ \chi_{21}^{(2)} & \chi_{22}^{(2)} & \chi_{23}^{(2)} & 0 & \chi_{25}^{(2)} & 0\\ 0 & 0 & 0 & \chi_{34}^{(2)} & 0 & \chi_{36}^{(2)}\end{bmatrix},$$

where $\chi_{14}^{(2)}=\chi_{25}^{(2)}=\chi_{36}^{(2)}$, $\chi_{23}^{(2)}=\chi_{34}^{(2)}$, $\chi_{16}^{(2)}=\chi_{21}^{(2)}$.

Therefore, in-plane polarization along the *b*- and *c*-axis are

$$P_b(2\omega)=E_b^2\chi_{22}^{(2)}+E_c^2\chi_{23}^{(2)} \quad (7)$$

$$P_c(2\omega)=2E_bE_c\chi_{23}^{(2)} \quad (8)$$

It should be noted the above expressions are given in terms of crystallographic axis (*a, b, c*). To transform them to the laboratory axes (*x, y, z*) as defined in above Figure S23, we assume the laboratory *z*-axis is at an angle θ from the crystallographic *c*-axis. Then, the in-plane polarization

along the *y*- and *z*-axis are

$$P_y(2\omega) = E_b^2\chi_{22}^{(2)} \cdot cos\theta + E_c^2\chi_{23}^{(2)} \cdot cos\theta - E_bE_c\chi_{23}^{(2)} \cdot sin\theta \quad (9)$$

$$P_z(2\omega) = E_b^2\chi_{22}^{(2)} \cdot sin\theta + E_c^2\chi_{23}^{(2)} \cdot sin\theta + 2E_bE_c\chi_{23}^{(2)} \cdot cos\theta \quad (10)$$

If we assume the electric filed E_ω polarized along the *z*-axis, then $E_c = E_\omega \cdot cos\theta$ and $E_c = E_\omega \cdot sin\theta$. Thus,

$$P_y(2\omega) = E_\omega^2(\chi_{23}^{(2)} \cdot cos^3\theta - 2\chi_{23}^{(2)} \cdot sin^2\theta cos\theta + \chi_{22}^{(2)} \cdot sin^2\theta cos\theta) \quad (11)$$

$$P_z(2\omega) = E_\omega^2(3\chi_{23}^{(2)} \cdot cos^2\theta sin\theta + \chi_{22}^{(2)} \cdot sin^3\theta). \quad (12)$$

Therefore, when we rotate the polarization of fundamental wave by an angle θ with the crystallographic *c*-axis, the parallel component of SHG intensity is

$$I_{2\omega}^{//} \propto |P_z(2\omega)|^2 = |E_\omega|^4(3\chi_{23}^{(2)} \cdot cos^2\theta + \chi_{22}^{(2)} \cdot sin^2\theta)^2 \cdot sin^2\theta \propto (3\chi_{23}^{(2)} \cdot cos^2\theta + \chi_{22}^{(2)} \cdot sin^2\theta)^2 \cdot sin^2\theta, \quad (13)$$

and the perpendicular component is

$$I_{2\omega}^{\perp} \propto \left|P_y(2\omega)\right|^2 \propto \left(\chi_{23}^{(2)} - 3\chi_{23}^{(2)} \cdot sin^2\theta + \chi_{22}^{(2)} \cdot sin^2\theta\right)^2 \cdot (1 - sin^2\theta). \quad (14)$$

The total SHG intensity $I_{2\omega}$ is

$$I_{2\omega} \propto (2\chi_{22}^{(2)} + 4\chi_{23}^{(2)}) \cdot \chi_{23}^{(2)} \cdot sin^2\theta + ((\chi_{22}^{(2)})^2 - 8(\chi_{23}^{(2)})^2) \cdot sin^4\theta + (\chi_{23}^{(2)})^2 \quad (15)$$

S5.3 Thickness-dependent SHG response

As shown in above Figure S24, our SHG experiments were performed in back reflection geometry (for samples on silicon substate). The coherence length is $\Delta L = \frac{\lambda_\omega}{4(n_\omega + n_{2\omega})}$=~48 nm,[9,10] where λ_ω=808 nm and n=~2.1 (Figure S11) are employed. Consequently, as shown in the Figures 3e,f in the main text, the SHG intensity scales quadratically with thickness (for thickness <30L (~20 nm)) as it is below the penetration depth (~$\Delta L/2 = \sim 24\ nm$) of SHG signal. For larger thickness (main

text, Figure 4h), two peaks occur at ~80L (~52 nm) and ~170L (~110 nm), respectively, due to interference effects.

To model the thickness dependent SHG intensity, we account for the surface/interface and bulk contributions (see Figure S24)[11]. The overall SHG intensity (P_2) can be expressed as $P_2 \propto |S(l) + B(l)|^2 \cdot {P_1}^2$, where *S(l)* and *B(l)* represent the surface and bulk contributions, respectively. We can write:

$$S(l) = \chi_S^{(2)}(R_{01} + T_{01}T_{10}R_{12}e^{2iKl} + {t_{10}}^2R_{12}T_{10}e^{2ikl}e^{iKl}) \quad (16)$$

$$B(l) = \chi_B^{(2)}l(T_{10}{t_{10}}^2R_{12}e^{2iKl} + {t_{10}}^2{r_{12}}^2T_{10}e^{2ikl}e^{iKl}) \quad (17)$$

where $r_{ij} = \frac{n_{\omega,i}-n_{\omega,j}}{n_{\omega,i}+n_{\omega,j}}$, $t_{ij} = \frac{2n_{\omega,i}}{n_{\omega,i}+n_{\omega,j}}$ are the Fresnel coefficients at fundamental wavelength, and $R_{ij} = \frac{n_{2\omega,i}-n_{2\omega,j}}{n_{2\omega,i}+n_{2\omega,j}}$, $T_{ij} = \frac{2n_{2\omega,i}}{n_{2\omega,i}+n_{2\omega,j}}$ at SH wavelength. Here 0, 1, 2 represent air, sample and SiO_2, respectively. $\chi_S^{(2)}$ and $\chi_B^{(2)}$ are the second-order nonlinear susceptibilities for the surface and bulk, respectively. $k = \frac{2\pi n_\omega}{\lambda_\omega}$ and $K = \frac{2\pi n_{2\omega}}{\lambda_{2\omega}}$ are the wavevectors at the fundamental and SH wavelengths, respectively. l is the sample thickness. To account for the effects due to a thin SiO_2 layer along with a high-reflection interface (SiO_2/Si) in the bottom, we consider the R_{12} and r_{12} in equations (16) and (17) as effective ones: $r_{12}^{eff} = t_{12}t_{21}r_{23}e^{i\frac{2\pi n_\omega}{\lambda_\omega}L} + r_{12}$, $R_{12}^{eff} = T_{12}T_{21}R_{23}e^{i\frac{2\pi n_{2\omega}}{\lambda_{2\omega}}L} + R_{12}$, where 3 represents bottom Si and L(=285 nm) is the SiO_2 thickness.

It's noteworthy that the coherence length in *transmission geometry*[12] is $\Delta L = \frac{\lambda_\omega}{4(n_{2\omega}-n_\omega)} = \sim 2\ \mu m$, implying a wider thickness range for monotonically increasing SHG could be expected in transmission geometry.

S5.4 Calculation of nonlinear coefficient and comparison with other materials

The SHG intensity can be expressed as

$$P_{2\omega} = \frac{8\pi^2 l^2 d^2}{{n_\omega}^2 n_{2\omega} {\lambda_\omega}^2 c\varepsilon_0} \frac{P_\omega^2}{\pi\omega_{10}^2} sinc^2(\Delta kl/2), \quad (18)$$

where P_ω and $P_{2\omega}$ are the excitation and SH intensity, n_ω and $n_{2\omega}$ the refractive index at fundamental and SHG wavelengths, l the thickness, d the effective second-order nonlinear coefficient, ω_{10} the waist radius of excitation laser, λ_ω the excitation wavelength, c the light speed and ε_0 the vacuum permittivity. So, at the same conditions (λ_ω and P_1), $P_{2\omega} \propto \frac{l^2 d^2}{{n_\omega}^2 n_{2\omega}}$. In other word, high conversion efficiency is not only facilitated by a large effective nonlinear coefficient but also by a higher interaction length as well as low refractive index (n~2.1 for $NbOCl_2$, while ~4 for WS_2)[13,14].

To calculate the second-order nonlinear coefficient, we took a *x*-cut $LiNbO_3$ film (500 nm) (on a 3-μm-thick SiO_2 buffer layer and a 500-μm fused silica substrate) as a standard sample for reference, of which the effective second-order nonlinear coefficient was taken as d=40 pm/V[15]. The conversion efficiency η_{LiNbO3} was measured to be ~$1.45*10^{-8}$ W^{-1} (considering a signal detecting efficiency of ~0.4% with our system). For monolayer WS_2, $sinc^2(\Delta kl/2)$~1, ${\chi^{(2)}}_{WS2}$ was measured and determined to be ~4 nm/V (or d~2 nm/V) and η_{WS2}~$4.2*10^{-11}$ W^{-1}.

As we discussed in S5.3 above, the interference effects will lead to complex thickness-dependence of the SHG efficiency. To estimate the material's intrinsic nonlinear coefficients of $NbOCl_2$, we choose flakes with thickness below the penetration depth and coherence length (~21 and ~48 nm, respectively, see S5.3) that is free from strong self-absorption and additional photonic effects. As shown in Figure 3g in main text, we measured and estimated the effective nonlinear coefficient d of different thickness and the values fall around 200 pm/V within a small range (when excited at 808 nm). It's interesting to note that the nonlinear coefficient shows a layer-independence (Figure 3g, main text), which is different from *2H*-TMDCs or *3R*-MoS_2[10]. Therefore, we take the

effective nonlinear coefficient d=~200 pm/V for intrinsic $NbOCl_2$. For 170L (~110 nm) $NbOCl_2$, the conversion efficiency was estimated to be η_{NbOCl2} ~8.2*10^{-9} W^{-1}. For 81L (~53 nm), η_{NbOCl2}~3.4*10^{-9} W^{-1}; for 30L (~20 nm), η_{NbOCl2}~1.3*10^{-10} W^{-1}.

To compare the nonlinear properties of $NbOCl_2$ with other materials (including both recently emerging 2D materials and traditional bulk crystals), we investigated and presented these data in Table S4 and summarized in Figure S27. For direct comparison of our results with the earlier works, we defined the conversion efficiency as $\eta = P_{2\omega}/[P_{\omega}]^2$. For emerging 2D materials, especially monolayer TMDCs, the reported nonlinear coefficients from different groups varied over 3-4 orders of magnitude, which are supposed to be mainly related with the sample quality and/or measuring conditions. As for our monolayer WS_2 sample, the measured nonlinear coefficient and conversion efficiency are both among the highest reported levels of TMDCs, indicating a high quality of our WS_2 sample that can serve as a good reference sample for comparison.

To gain a general view from the comparison, the nonlinear coefficient $\chi^{(2)}$ of $NbOCl_2$ lies between the emerging 2D materials and traditionally bulky crystals (Figure S27). Although the $\chi^{(2)}$ of TMDC monolayers are very high, their conversion efficiency η are rather limited by the vanishing thickness and not scalable with thickness. While for bulky crystals, their conversion efficiency η can be achieved at a high level by controlling thickness, but their nonlinear coefficient $\chi^{(2)}$ are 1-2 orders lower than that of $NbOCl_2$. This can be evidenced by the fact that a 110 nm $NbOCl_2$ can show an almost comparable conversion efficiency to that of a 500 nm $LiNbO_3$ film (Figure S27). Therefore, the $NbOCl_2$ crystal bridges the gap between TMDCs and bulky crystals for relatively high $\chi^{(2)}$ (*vs* bulk crystals) while scalable η (*vs* TMDCs).

It's also noted that some 2D materials with specific crystal structures also show a scalable SHG

response. Among them, *3R*-MoS_2 is a typical example, but the SHG intensity scales only up to 6 layers before decrease again[16,17] Besides, the *3R* phase is metastable and difficult to synthesize. Others like ε-InSe/GaSe suffer from structural or chemical stabilities though with a noncentrosymmetric structure and moderate $\chi^{(2)}$. The 2D magnet CrI_3 shows a high $\chi^{(2)}$, but only works at 4 K and in bilayer form[18].

S6. Additional information for SPDC experiments

S6.1 Calculation of coincidence rate and estimation of detection efficiency of SPDC experiments

The photon pair coincidence counting rate C=A*CAR, where A is the accidental coincidence rate, and CAR is coincidences-to-accidentals ratio. The accidental rate A=N_1*N_2*T_c, where N_1 and N_2 are the counts of the two detectors respectively, and T_c is the effective time resolution. The coincidences-to-accidentals ratio CAR=$g^{(2)}(0)$-1.

For the SPDC experiments, the total detection efficiency can be estimated as follows,

$$\eta^{total}_{signal/idler} = \eta^{obj,50x}_{signal/idler} \times \eta^{Pol.}_{signal/idler} \times \eta^{FC}_{signal/idler} \times \eta^{BS}_{signal/idler} \times \eta^{SPD}_{signal/idler} \times \eta^{BP}_{signal/idler} = \sim 0.1\%,$$

where $\eta^{obj,50x}_{signal/idler} = 0.7^2$, $\eta^{Pol.}_{signal/idler} = 0.8^2$ are the photon pair transmissions through the objective and polarizer, respectively, $\eta^{FC}_{signal/idler} = 0.7^2$ is the efficiency of fiber coupler, $\eta^{BS}_{signal/idler} = 0.8^2 * 0.5 = 0.32$ is the efficiency of beam splitter, and $\eta^{SPD}_{signal/idler} = 0.6^2$ is the quantum efficiency of SPDs (~0.6 around the degenerate SPDC wavelength). Here, $\eta^{BP}_{signal/idler} = 0.98^2 * 0.05 = 0.048$ includes the bandpass filter transmission (0.98) and the

filtered spectral weight of actual SPDC spectrum (taken as a moderate value of ~0.05 for a 10-nm wide bandpass filter). We should stress that spectral weight estimation is conservative as the bi-photon bandwidth is at least 200 nm based on our experiments (see below in Figure S29), which is a feature of thin film SPDC source[19].

Specifically, with an excitation of 59 mW, the detected photon pair coincidence rate is ~86 Hz (Figure 4g, main text) corresponding to an actually photon pair generation rate of at least ~86000 Hz ($C/\eta_{signal/idler}^{total}$), which is well higher than that of recently reported AlGaAs nanoantenna (35 Hz)[20]. And the coincidence rate can be further enhanced by increasing excitation power (considering the linear scaling with excitation power) and optimizing the film thickness or excitation conditions (higher signal-to-noise ratio).

To inspect the intrinsic material potentials of chi2 medium as SPDC source, the figure of merit (FoM) for SPDC efficiency is adopted for comparison under the same interaction volume and pump power level. The FoM for SPDC efficiency is determined by taking the pump energy stored by the flake into account, i.e., normalized by $V_0 I_p Q_p$, where V_0 is the volume of the nonlinear materials responsible for SPDC, I_p is the incident pump intensity at the input, and Q_p is the quality factor at the pump wavelength[20]. For a 150 nm thick flake, excitation power 59 mW and Q_p~1, the figure of merit for SPDC efficiency is estimated to be ~9800 GHz W^{-1} m^{-1}, which is of tremendous advantage among conventional on-chip and bulk photon-pair media, including BBO crystal (~10^{-4} GHz W^{-1} m^{-1})[21], AlN waveguide (~0.136 GHz W^{-1} m^{-1})[22], AlGaAs nanoantenna (~1.4 GHz W^{-1} m^{-1})[20], GaP thin film (~267.9 GHz W^{-1} m^{-1})[19] and $LiNbO_3$ film (~5000 GHz W^{-1} m^{-1})[19].

It needs to note that the absolute brightness of traditional bulk SPDC sources (such as BBO crystal and periodically polarized $LiNbO_3$ waveguides) is higher than our ultrathin SPDC source

due to considerable larger thickness and further elaborately engineered phase-matching conditions. However, the superior optical nonlinearity in $NbOCl_2$ over other van der Waals materials enables it a highly competitive choice in constructing chip-integrated SPDC source via facile van der Waals integration. On one hand, the brightness of SPDC source is just one of the considerations for practical applications where preparation and manipulation of quantum entanglement states are also essential and the facile integration with other photonic structures (i.e., metasurfaces, cavities or waveguides) will greatly facilitate these aspects that are impossible or difficult for bulky counterparts. One the other hand, the brightness of our ultrathin SPDC source could also be considerably enhanced by coupling (integrating) with waveguides, cavities or metasurfaces.

S6.2 Pump power and film thickness dependent photon-pair generation rate

The dependence of photon pair generation rate on pump power and film thickness can be descripted[23] as

$$r_{SPDC} \propto \frac{4d_{eff}^2 P_p L^2}{9\varepsilon_0^2 c^2 A_{eff}} sinc^2(\frac{\Delta kL}{2}), \quad (19)$$

where r_{SPDC} is the photon pair generation rate, P_p is the pump power, A_{eff} is the mode interaction overlap area and can be taken as the laser beam size on film, L is film thickness, d_{eff} is the effective nonlinear coefficient. The *sinc* term represents the nonperfect phase-matching among the wave components. Therefore, the photon pair generation rate scales linearly with pump power and quadratically with thickness, provided that the thickness of flakes considered here are all within the coherence length ($L_c = \pi/\Delta k = \sim 2\ \mu m$, in transmission geometry) and photon pair are always generated in phase.

S6.3 Additional data

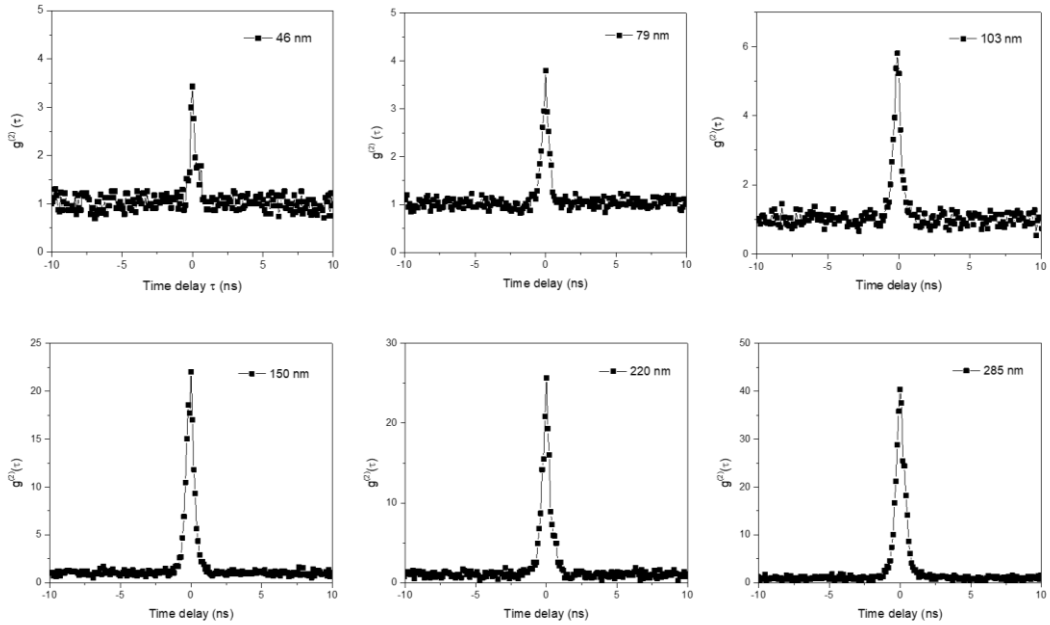

Figure S28 | Typical normalized second-order correlation functions for flakes of different thicknesses, with a pump power of 3 mW.

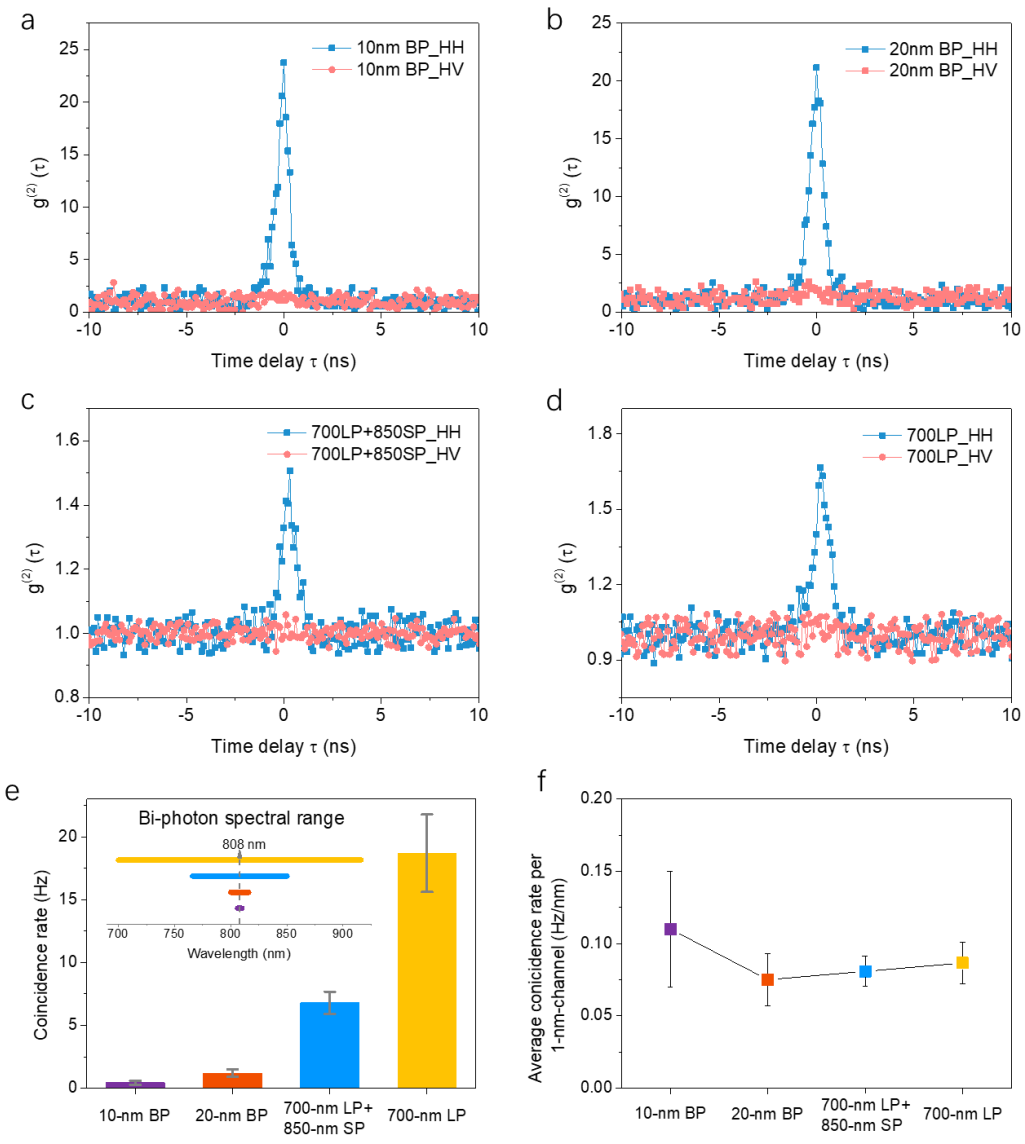

Figure S29 | Information on the bi-photon bandwidth. (a-d) SPDC results measured with different filter configurations. The polarization of pump is kept along the crystallographic b-axis (noted as H) while the collection polarization of SPDC photons is either along b-axis (HH) or c-axis (HV). (e) Measured coincidence rate with different filter configurations. (f) Average coincidence rate per 1-nm channel with different filter configurations. These results reveal a broad and relatively flat bi-photon bandwidth in our sample.

S7. Supplementary tables

Table S1 | Comparison of bandgap evolution of various 2D materials

Materials	Bandgap/eV							Evolution $(E_g^{1L}\text{-}E_g^{bulk})/E_g^{1L}$	Reference
	1L	2L	3L	4L	10L	18L	bulk		
MoS_2	1.9	1.66	1.34				1.2	36.8%	Ref. 24
$MoSe_2$	1.58	1.46					1.2	24.1%	Ref. 5
WS_2	2.03	1.75	1.58	1.5			1.47	38.1%	Ref. 24-26
WSe_2	1.68	1.53	1.43				1.25	25.6%	Ref. 5
$MoTe_2$	1.08	1.05	1.03	1			0.93	13.9%	Ref. 27
Black phosphorus	1.73	1.15	0.83	0.75			0.35	79.8%	Ref. 28
ReS_2	1.6	1.52	1.5				1.5	6.25%	Ref. 5
$NbOCl_2$ (*HSE*)	1.99	1.98	1.98				1.98	0.5%	This work
$NbOCl_2$ (*GW*)	2.27						2.21	2.6%	This work
$NbOCl_2$ (*Exp.*)*		1.62		1.60	1.60	1.61	1.60	1.2%	This work

*The experimental value is the absorption onset energy derived from EELS data.

Table S2 | Calculated Raman-active and infrared (IR)-active phonon modes, and experimental Raman-active phonon modes of $NbOCl_2$ with their irreducible representations at room temperature.

Phonon mode	Activity	Calculated energy [cm^{-1}]	Calculated intensity [a.u.]	Experimental energy [cm^{-1}]	Symmetry
1	Raman	0	5.8		A
2	Raman	0	2.6		B
3	Raman	0	0.0		B
4	Raman+IR	109.0	0.3		B
5	Raman	113.6	2.1		A
6	Raman+IR	115.8	0.8		B
7	Raman+IR	127.1	11.1		A
8	Raman+IR	133.3	29.7		B
9	Raman+IR	151.2	1026.3	161.9(P1)	A

10	Raman+IR	161.9	2036.4	176.7(P2)	A
11	Raman+IR	173.3	60.5		A
12	Raman+IR	209.5	99.1		B
13	Raman+IR	230.7	27.5		B
14	Raman	242.2	20.3		A
15	Raman+IR	249.1	4.1		B
16	Raman+IR	255.2	2007.2		A
17	Raman+IR	264.0	1.6		B
18	Raman	280.1	231.4		B
19	Raman+IR	282.4	1565.8	298.0(P3)	A
20	Raman+IR	297.8	58.4		A
21	Raman+IR	323.6	1748.4	341.4(P4)	A
22	Raman+IR	369.1	5.6		B
23	Raman+IR	580.5	5.0		B
24	Raman+IR	587.2	13823.1	669.5(P5)	A

Table S3 | Comparison of pressure and temperature coefficient of the most prominent out-of-plane Raman mode of $NbOCl_2$ and other typical 2D materials.

Materials	Raman mode	dω/dP (cm^{-1}/Gpa)	χ (cm^{-1}/K)
Graphene	G	1.99[29]	-0.0162[30]
MoS_2	A_{1g}	2.7[31]	-0.0123[31]
$MoSe_2$	A_{1g}	2.4[32]	-0.0054[33]
WSe_2	A_{1g}	1.52[34]	-0.0032[33]
WS_2	A_{1g}	3.0[35]	-0.0103[36]
$MoTe_2$	A_{1g}	2.5[37]	-0.0081[38]
Black Phosphorus	A_g^1	4.39[39]	-0.023[40]
SnS	A_g	-	-0.016[41]
SnSe	A_g^1	2.56[42]	-0.0091[43]
ReS_2	A_g-like	1[5]	-0.0083[44]
$NbOCl_2$	A_2	0.73[this work]	-0.0088[this work]

Table S4 | Typical SHG processes in various 2D materials and bulk crystals

Material	SH wavelength [nm]	$\chi^{(2)}$ [pm/V]*	η [W^{-1}]**	Thickness***	Reference
MoS_2	500	120	-	ML	Ref. 45
	780	29	$2.4x10^{-14}$	ML	Ref. 46
	500	5000	$1x10^{-12}$	ML	Ref. 47
	680	40	-	ML	Ref. 48
	405	311	-	ML	Ref. 49

	440	300	-	ML	Ref. 50
	780 (non-resonant)	5	7.5×10^{-16}	ML	Ref. 51
$MoSe_2$	600-900	10-50	-	ML	Ref. 48
	775	4500	-	ML	Ref. 52
	460	300	-	ML	Ref. 50
	780	37	3.5×10^{-14}	ML	Ref. 51
WS_2	415	4500	-	ML	Ref. 53
	560	680	-	ML	Ref. 54
	440	300	-	ML	Ref. 50
	404	4000	1.6×10^{-13}	ML	This work
	780 (non-resonant)	16.2	0.67×10^{-14}	ML	Ref. 51
WSe_2	400	248	1.4×10^{-14}	ML	Ref. 55
	740	62	5×10^{-13}	ML	Ref. 56
	408	5000	-	ML	Ref. 57
	425	360	-	ML	Ref. 50
	780 (non-resonant)	16.5	0.67×10^{-14}	ML	Ref. 51
$MoTe_2$	500	50	-	ML/FL	Ref. 58
h-BN	405	20	-	ML	Ref. 49
	400	40	-	ML	Ref. 59
GaSe	780	18	-	9L	Ref. 60
	605	140	-	bulk	Ref. 61
	400	30	-	2-10L	Ref. 61
GaTe	760	1.15	4.5×10^{-17}	57 nm	Ref. 62
In_2Se_3	800	40	-	ML	Ref. 63
$PdSe_2$	440	51.7	-	4L	Ref. 64
$AgInP_2S_6$	400	<50	-	ML	Ref. 65
CrI_3	450	2000	-	2L(4K)	Ref. 18
3R-MoS_2	600	30	-	bulk	Ref. 10
GaAs	1533	119	-	bulk	Ref. 66
β-BaB_2O_4 (BBO)	532	2	-	bulk	Ref. 15
α-SiO_2 (quartz)	529	0.8	-	bulk	Ref. 56
AlN	775	4.7	-	bulk	Ref. 22
GaP	1313	36.8	-	bulk	Ref. 66
$LiNbO_3$	404	40[57]	5.5×10^{-11}	500 nm	This work
$BaTiO_3$	450	30	-	bulk	Ref. 67
$NbOCl_2$	404	400	3.12×10^{-11}	110 nm	This work

* Note $\chi^{(2)} = 2d_{eff}$, where d_{eff} is the effective second-order nonlinear coefficient.

** For direct comparison among different materials, the conversion efficiency is defined as $\eta = P_{2\omega}/[P_{\omega}]^2$, where P_{ω} and $P_{2\omega}$ are the power of pump and SHG respectively.

***L=layer, ML=monolayer, FL=few-layer.

References

1 Bjorkman, T., Gulans, A., Krasheninnikov, A. V. & Nieminen, R. M. van der Waals bonding in layered compounds from advanced density-functional first-principles calculations. *Phys. Rev. Lett.* **108**, 235502 (2012).

2 Peng, H., Yang, Z.-H., Perdew, J. P. & Sun, J. Versatile van der Waals Density Functional Based on a Meta-Generalized Gradient Approximation. *Phys. Rev. X* **6**, 041005 (2016).

3 Mounet, N. *et al.* Two-dimensional materials from high-throughput computational exfoliation of experimentally known compounds. *Nat. Nanotechnol.* **13**, 246-252 (2018).

4 Jia, Y., Zhao, M., Gou, G., Zeng, X. C. & Li, J. Niobium oxide dihalides $NbOX_2$: a new family of two-dimensional van der Waals layered materials with intrinsic ferroelectricity and antiferroelectricity. *Nanoscale Horiz.* **4**, 1113-1123 (2019).

5 Tongay, S. *et al.* Monolayer behaviour in bulk ReS_2 due to electronic and vibrational decoupling. *Nat. Commun.* **5**, 3252 (2014).

6 Yan, H.-J. *et al.* Investigation of weak interlayer coupling in 2D layered GeS_2 from theory to experiment. *Nano Res.* **15**, 1013 (2022).

7 Yang, Y. *et al.* Weak interlayer interaction in 2D anisotropic $GeSe_2$. *Adv. Sci.* **6**, 1801810 (2019).

8 Calizo, I., Balandin, A. A., Bao, W., Miao, F. & Lau, C. N. Temperature dependence of the Raman spectra of graphene and graphene multilayers. *Nano Lett.* **7**, 2645-2649 (2007).

9 Mishina, E. *et al.* Observation of two polytypes of MoS_2 ultrathin layers studied by second harmonic generation microscopy and photoluminescence. *Appl. Phys. Lett.* **106**, 131901 (2015).

10 Shi, J. *et al.* 3R MoS_2 with Broken Inversion Symmetry: A Promising Ultrathin Nonlinear Optical Device. *Adv. Mater.* **29**, 1701486 (2017).

11 Deckoff-Jones, S. *et al.* Observing the interplay between surface and bulk optical nonlinearities in thin van der Waals crystals. *Sci. Rep.* **6**, 22620 (2016).

12 Piltch, M. S., Eckhardt, R. & Hinsley, R. Determination of the nonlinear optical coefficient and SHG coherence length for crystal single Zinc Selenide. *Opt. Common.* **22**, 239 (1977).

13 Zhou, X. *et al.* Strong Second-Harmonic Generation in Atomic Layered GaSe. *J. Am. Chem. Soc.* **137**, 7994-7997 (2015).

14 Autere, A. *et al.* Nonlinear Optics with 2D Layered Materials. *Adv. Mater.* **30**, 1705963 (2018).

15 Okoth, C., Cavanna, A., Santiago-Cruz, T. & Chekhova, M. V. Microscale Generation of Entangled Photons without Momentum Conservation. *Phys. Rev. Lett.* **123**, 263602 (2019).

16 Zhao, M. *et al.* Atomically phase-matched second-harmonic generation in a 2D crystal. *Light: Sci. & Appl.* **5**, e16131 (2016).

17 Zhang, J., Zhao, W., Yu, P., Yang, G. & Liu, Z. Second harmonic generation in 2D layered materials. *2D Mater.* **7**, 042002 (2020).

18 Sun, Z. *et al.* Giant nonreciprocal second-harmonic generation from antiferromagnetic bilayer CrI_3. *Nature* **572**, 497-501 (2019).

19 Santiago-Cruz, T., Sultanov, V., Zhang, H., Krivitsky, L. A. & Chekhova, M. V. Entangled photons from subwavelength nonlinear films. *Opt. Lett.* **46**, 653-656 (2021).

20 Marino, G. et al. Spontaneous photon-pair generation from a dielectric nanoantenna. *Optica* **6**, 1416 (2019).

21 Kwiat, P. G. *et al*. New high-intensity source of polarization-entangled photon pairs. *Phys. Rev.*

Lett. **75**, 4337-4341 (1995).

22 Guo, X. *et al.* Parametric down-conversion photon-pair source on a nanophotonic chip. *Light Sci. Appl.* **6**, e16249 (2017).

23 Wang, Y., D. Jons, K. & Sun, Z. Integrated photon-pair sources with nonlinear optics. *Appl. Phys. Rev.* **8**, 011314 (2021).

24 Kuc, A., Zibouche, N. & Heine, T. Influence of quantum confinement on the electronic structure of the transition metal sulfide TS_2. *Phys. Rev. B* **83** (2011).

25 Liu, Y., Hu, X., Wang, T. & Liu, D. Reduced binding energy and layer-dependent exciton dynamics in monolayer and multilayer WS_2. *ACS Nano* **13**, 14416 (2019).

26 Cong, C., Shang, J., Wang, Y. & Yu, T. Optical properties of 2D semiconductor WS_2. *Adv. Opt. Mater.* **6**, 1700767 (2018).

27 Ruppert, C., Aslan, O. B. & Heinz, T. F. Optical properties and band gap of single- and few-layer $MoTe_2$ crystals. *Nano Lett.* **14**, 6231-6236 (2014).

28 Li, L. *et al.* Direct observation of the layer-dependent electronic structure in phosphorene. *Nat. Nanotechnol.* **12**, 21-25 (2017).

29 Proctor, J. E. *et al.* High-pressure Raman spectroscopy of graphene. *Phy. Rev. B* **80**, 073408 (2009).

30 Calizo, I., Balandin, A. A., Bao, W., Miao, F. & Lau., C. N. Temperature dependence of the Raman spectra of graphene and graphene multilayers. *Nano Lett.* **7**, 2645-2649 (2007).

31 Li, X. *et al.* Pressure and temperature-dependent Raman spcetra of MoS_2 film. *Appl. Phys. Lett.* **109**, 242101 (2016).

32 Yang, L. *et al.* Pressure-induced metallization in $MoSe_2$ under different pressure conditions. *RSC Adv.* **9**, 5794-5803 (2019).

33 Late, D. J., Shirodkar, S. N., Waghmare, U. V., Dravid, V. P. & Rao, C. N. Thermal expansion, anharmonicity and temperature-dependent Raman spectra of single- and few-layer $MoSe_2$ and WSe_2. *ChemPhysChem* **15**, 1592-1598 (2014).

34 Wang, X. *et al.* Pressure-induced iso-structural phase transition and metallization in WSe_2. *Sci. Re.* **7**, 46694 (2017).

35 Kim, J.-S. *et al.* High pressure Raman study of layered $Mo_{0.5}W_{0.5}S_2$ ternary compound. *2D Mater.* **3**, 025003 (2016).

36 Hu, Z. *et al.* Temperature dependent Raman and photoluminescence of vertical WS_2/MoS_2 monolayer heterostructures. *Sci. Bull.* **62**, 16-21 (2017).

37 Qi, Y. *et al.* Superconductivity in Weyl semimetal candidate $MoTe_2$. *Nat. Commun.* **7**, 11038 (2016).

38 Zhang, H. *et al.* High temperature Raman investigation of few-layer $MoTe_2$. *Appl. Phys. Lett.* **108**, 091902 (2016).

39 Gupta, S. N. *et al.* Raman anomalies as signatures of pressure induced electronic topological and structural transitions in black phosphorus: Experiments and theory. *Phys. Rev. B* **96**, 094104 (2017).

40 Zhang, S. *et al.* Extraordinary photoluminescence and strong temperature/angle-dependent Raman responses in few-layer phosphorene. *ACS Nano* **8**, 9590-9596 (2014).

41 Xia, J. *et al.* Physical vapor deposition synthesis of two-dimensional orthorhombic SnS flakes with strong angle/temperature-dependent Raman responses. *Nanoscale* **8**, 2063-2070 (2016).

42 Zhang, J. *et al.* Plasma-assisted synthesis and pressure-induced structural transition of single-

crystalline SnSe nanosheets. *Nanoscale* **7**, 10807-10816 (2015).

43 Gong, X. *et al.* Temperature dependence of Raman scattering in single crystal SnSe. *Vib. Spectrosc.* **107**, 103034 (2020).

44 Jiang, S. *et al.* Temperature-dependent Raman spectroscopy studies of the interface coupling effect of monolayer $ReSe_2$ single crystals on Au foils. *Nanotechnology* **29**, 204003 (2018).

45 Malard, L. M., Alencar, T. V., Barboza, A. P. M., Mak, K. F. & de Paula, A. M. Observation of intense second harmonic generation from MoS_2 atomic crystals. *Phys. Rev. B* **87**, 201401(R) (2013).

46 Woodward, R. I. *et al.* Characterization of the second- and third-order nonlinear optical susceptibilities of monolayer MoS_2 using multiphoton microscopy. *2D Mater.* **4**, 011006 (2016).

47 Kumar, N. *et al.* Second harmonic microscopy of monolayer MoS_2. *Phys. Rev. B* **87**, 161403(R) (2013).

48 Le, C. T. *et al.* Nonlinear optical characteristics of monolayer $MoSe_2$. *Annalen der Physik* **528**, 551-559 (2016).

49 Li, Y. *et al.* Probing symmetry properties of few-layer MoS_2 and h-BN by optical second-harmonic generation. *Nano Lett.* **13**, 3329-3333 (2013).

50 Yao, K. *et al.* Continuous Wave Sum Frequency Generation and Imaging of Monolayer and Heterobilayer Two-Dimensional Semiconductors. *ACS Nano* **14**, 708-714 (2020).

51 Autere, A. *et al.* Optical harmonic generation in monolayer group-VI transition metal dichalcogenides. *Phys. Rev. B* **98**, 115426 (2018).

52 Chen, H. *et al.* Enhanced second-harmonic generation from two-dimensional $MoSe_2$ on a silicon waveguide. *Light: Sci. & Appl.* **6**, e17060 (2017).

53 Janisch, C. *et al.* Extraordinary Second Harmonic Generation in tungsten disulfide monolayers. *Sci. Rep.* **4**, 5530 (2014).

54 Fan, X. *et al.* Broken Symmetry Induced Strong Nonlinear Optical Effects in Spiral WS_2 Nanosheets. *ACS Nano* **11**, 4892-4898 (2017).

55 Wang, Z. *et al.* Selectively Plasmon-Enhanced Second-Harmonic Generation from Monolayer Tungsten Diselenide on Flexible Substrates. *ACS Nano* **12**, 1859-1867 (2018).

56 Seyler, K. L. *et al.* Electrical control of second-harmonic generation in a WSe_2 monolayer transistor. *Nat. Nanotechnol.* **10**, 407-411 (2015).

57 Ribeiro-Soares, J. *et al.* Second Harmonic Generation in WSe_2. *2D Mater.* **2**, 045015 (2015).

58 Beams, R. *et al.* Characterization of Few-Layer 1T' $MoTe_2$ by Polarization-Resolved Second Harmonic Generation and Raman Scattering. *ACS Nano* **10**, 9626-9636 (2016).

59 Grüning, M. & Attaccalite, C. Second harmonic generation in *h*-BN and MoS_2 monolayers: Role of electron-hole interaction. *Phys. Rev. B* **89**, 081102(R) (2014).

60 Karvonen, L. *et al.* Investigation of second- and third-harmonic generation in few-layer gallium selenide by multiphoton microscopy. *Sci. Rep.* **5**, 10334 (2015).

61 Jie, W. *et al.* Layer-dependent nonlinear optical properties and stability of non-centrosymmetric modification in few-layer GaSe sheets. *Angew. Chem. Int. Ed.* **54**, 1185-1189 (2015).

62 Susoma, J. *et al*. Second and third harmonic generation in few-layer gallium telluride characterized by multiphoton microscopy. *Appl. Phys. Lett.* **108**, 073103 (2016).

63 Lin, J. *et al.* Indium selenide monolayer: a two-dimensional material with strong second harmonic generation. *CrystEngComm* **20**, 2573-2582 (2018).

64 Yu, J. *et al.* Giant nonlinear optical activity in two-dimensional palladium diselenide. *Nat.*

Commun. **12**, 1083 (2021).

65 Wang, Z. *et al*. Second-harmonic generation in quanternary atomically thin layered $AgInP_2S_6$ crystals. *Appl. Phys. Lett.* **109**, 123103 (2016).

66 Shoji, I., Kondo, T., Kitamoto, A., Shirane, M. & Ito, R. Absolute scale of second-order nonlinear-optical coefficients. *J. Opt. Soc. Am. B* **14**, 2268 (1997).

67 Wu, L. *et al*. Giant anisotropic nonlinear optical response in transition metal monopnictide Weyl semimetals. *Nat. Phys.* **13**, 350-355 (2016).